Fast and slow architectures of cortical dynamics in human brain

Yuhan Lu[1,2,3,†], Zhuoran Li[4,†], Hangze Mao[5,†], Qinsiyuan Lyu[2,3], Chen Yao[6], Junxi Chen[7], Louis Tao[8], Zhuo-Cheng Xiao[1,3,9]*, Xing Tian[1,3,*]

[1]Division of Arts and Sciences, New York University Shanghai, Shanghai 200122, China

[2]Shanghai Key Laboratory of Brain Functional Genomics (Ministry of Education), School of Psychology and Cognitive Science, East China Normal University, Shanghai 200062, China

[3]NYU-ECNU Institute of Brain and Cognitive Science, New York University Shanghai, Shanghai 200062, China

[4]Center for Quantitative Biology, Academy for Advanced Interdisciplinary Studies, Peking University, Beijing, 100871, China

[5]School of Medical Technology and Information Engineering, Zhejiang Chinese Medical University, Hangzhou 310053, China

[6]Department of Neurosurgery, the First Affiliated Hospital of Shenzhen University, Shenzhen Second People's Hospital, Shenzhen Clinical Research Center for Neurological Diseases, Shenzhen 518035, China.

[7]Department of Neurosurgery, Guangzhou Sanjiu Brain Hospital, Guanzhou 510510, China

[8]Center for Bioinformatics, National Laboratory of Protein Engineering and Plant Genetic Engineering, School of Life Sciences, Peking University, Beijing 100871, China

[9]NYU-ECNU Institute of Mathematical Sciences, New York University Shanghai, Shanghai 200062, China

[†]These authors have contributed equally to this work.

***Corresponding author:**

Xing Tian, E-mail: xing.tian@nyu.edu

Zhuo-Cheng Xiao, E-mail: xiao.zc@nyu.edu

Abstract

The most critical attribute of the brain is its ability to coordinate perception, thoughts, and action across different timescales. A prominent theory holds that the cortex is organized along a unidimensional hierarchy, where higher-order regions operate over longer intrinsic timescales than sensory areas, a view inferred from analytical methods that assume a single, dominant timescale per region. However, whether cortical dynamics are governed by such a singular hierarchy, or instead by multiple concurrent timescales, has remained unclear due to this fundamental methodological constraint. Here, developing an assumption-free spectral analysis of human intracranial recordings, we discover a fundamental dissociation: cortical dynamics are organized into a fast spectral component (~10-100 Hz) and a slow component (~1-10 Hz). Crucially, only the fast component spatially recapitulates the classic sensory-to-transmodal functional gradient, whereas the slow component lacks gradient and is coupled to cardiac-related neural activity. This dual-timescale architecture, stable across distinct conscious states, demonstrates human cortical dynamics are organized into parallel processing channels, not a single temporal hierarchy. This framework provides a new foundation for understanding dynamical subsystems that link to brain physiology and cognition.

Main

A fundamental challenge in neuroscience is to understand how the brain supports computations across vastly different timescales, from rapid sensory processing to sustained cognitive integration[1-4]. A dominant framework proposes that this multiscale capacity is embedded in a unidimensional cortical hierarchy, where a gradual transition from sensory to transmodal regions corresponds to a monotonic increase in a single, intrinsic neural timescale[5-11]. This parsimonious model, however, rests on a critical methodological simplification: the reduction of local spectral dynamics to one dominant timescale, such as autocorrelation decay[8,9,12-17] or spectral knee frequency[18-22]. This reduction is directly challenged by evidence that local circuits can operate across multiple, parallel timescales concurrently[21-24], where the single-timescale fitting cannot capture (**Fig. 1a**). Consequently, disparate techniques (fMRI, MEG/LFP, spiking) are each limited to distinct temporal ranges, extracting only a modality-specific "dominate" timescale that precludes reconstruction of the brain's full multiscale architecture. A pivotal question therefore remains unresolved (**Fig. 1b**): does the brain implement its hierarchy through a singular gradient of timescales, or through dissociable temporal components that are selectively embedded within its architecture? Answering this will define the brain's fundamental multiscale architecture as the temporal infrastructure within which all neural computations unfold, and whose alterations underpin shifts from healthy cognition to disease.

Here, we develop an assumption-free method that directly quantifies whether one or two timescales govern local dynamics. Applied to large-scale human stereo-electroencephalography (sEEG, n = 175), which records local field potentials with continuous, wideband spectral window, we reveal a cortex-wide organization of dissociable fast and slow temporal components that is stable across conscious states. Crucially, we demonstrate that these components obey distinct organizing principles, with only the fast timescales recapitulating the canonical cortical hierarchy. It suggests a multiscale computational infrastructure of the human cortex.

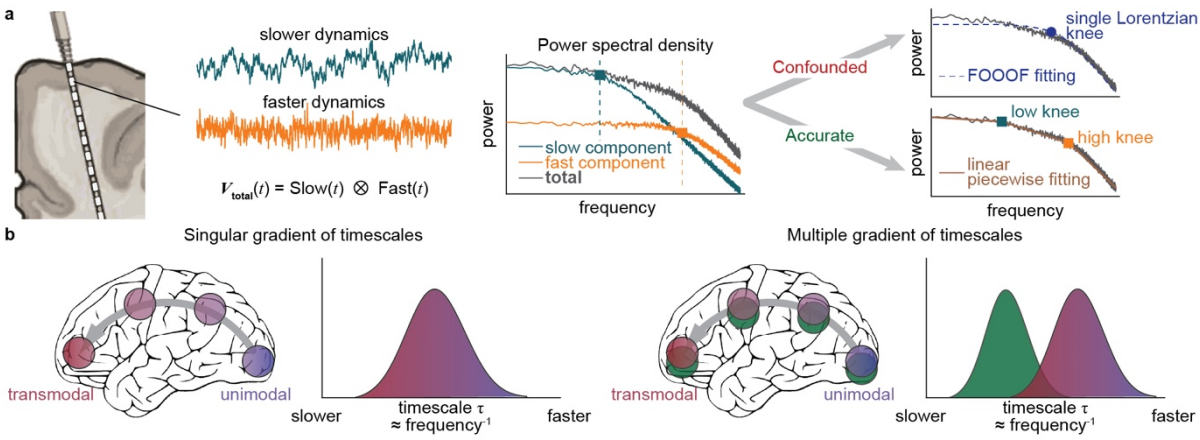

Figure 1. Methodological assumptions lead to distinct theoretical hypotheses. **a,** Local cortical activity can comprise concurrent slow and fast dynamics. Reducing the spectrum to a single characteristic timescale (single-knee fit) can conflate components and

yield an intermediate, biased knee, whereas fitting without prespecifying the number of knees can dissociate slow and fast components.
b, Competing hypotheses for cortex-wide timescale organization. Single-gradient model: one monotonic sensory-to-transmodal gradient in intrinsic timescale. Dissociation model: parallel slow and fast components imply multiple temporal subsystems.

Piecewise linear fitting resolves multiple spectral knees

A fundamental limitation of prevailing methods was their a priori assumption of a single spectral knee, which systematically obscured the potential existence of multiple, concurrent neural timescales. To overcome this constraint, we developed an assumption-free fitting procedure based on a core biophysical principle: distinct neural timescales manifested in the power spectrum as successive power-law regimes, each appearing as a linear-like segment in log-log space. By identifying these segments without presupposing their number, our piecewise-linear fitting algorithm directly recovered the true spectral bend points (**Fig. 2a**, left).

We validated the algorithm on simulated spectra with known configurations (0, 1, or 2 knees) and different levels of noise. Our piecewise linear fitting procedure accurately recovered the true number of knees across all conditions: it did not overfit spectra without a knee, correctly identified a single breakpoint in one-knee spectra, and cleanly decomposed two-knee spectra into distinct low- and high-frequency components that were visually apparent in the data (**Fig. 2a**). When subjected to increasing levels of empirically plausible noise, the procedure remained stable, with the error in recovered knee frequency staying below ~1 Hz and the overall model fit maintaining an $R^2 > 0.99$ (**Fig. 2b**). These results demonstrated that the method was sensitive to the presence of multiple components and robust under noisy conditions.

To ensure that the fitted knees reflect genuine neural dynamics rather than methodological artifacts[25-27], we conducted two essential controls for the analysis pipeline. First, we systematically compared methods for removing oscillatory components from PSD and found that Irregular resampling auto-spectral analysis (IRASA[28]) provided more robust aperiodic estimates than the widely-used FOOOF[20] toolkit in the presence of multiple spectral knees, preserving the true 1/f curvature and knee locations (**Fig. S1**). Second, we quantified the fundamental constraint imposed by Welch window length (see related discussion[17,29-32]), identifying the minimum data required to reliably resolve multiple timescales. (**Fig. S2**). These validations established that the core findings presented hereafter rested on a robust and unbiased methodological foundation.

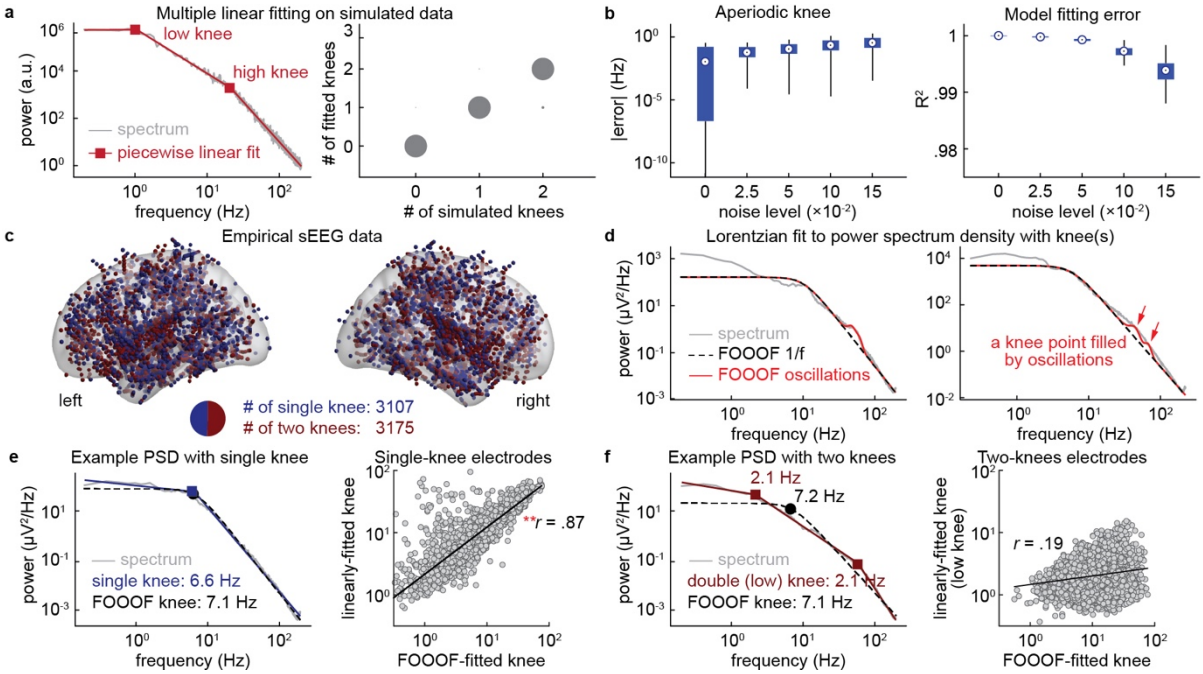

Figure 2. A robust piecewise linear fitting method resolves multiple neural timescales overlooked by standard approaches.

a, Our piecewise fitting procedure was validated on simulated power spectra with known configurations. It correctly decomposing double-knee spectra into distinct low- and high-frequency components (red squares; Left panel) and accurately recovered the true number of spectral knees (0, 1, or 2; shown as the area of grey circles; Right panel).

b, The algorithm demonstrated numerical robustness under empirically plausible noise levels, maintaining low knee-frequency error (<1 Hz) and high goodness-of-fit ($R^2 > 0.99$).

c, Application to human sEEG data (n = 136 subjects) revealed that neural spectra are bimodal: approximately half of all cortical electrodes are best described by a single knee, while the other half are two knees.

d, PSD examples illustrate that FOOOF can well separate 1/f and oscillatory components in the one-knee neuronal system (Left panel). In contrast, in the two-knees neuronal system, high-frequency spectral knee can be masked by oscillatory components (red arrows; Right panel).

e, In spectra with single-knee neuronal system, our method and the FOOOF toolkit produced nearly identical estimates (n = 3,107 electrodes; r = 0.87).

f, In spectra with two-knees neuronal system, FOOOF is supposed to capture the lowest, dominate knee. But FOOOF-fitted knees show no agreement with the slowest knees identified by the piecewise method (n = 3,175 electrodes; r = 0.19), suggesting that fitting a single Lorentzian function obscures the true timescale estimate.

Systematic errors introduced by single-knee fitting in human cortex

We next applied our method to human sEEG recordings, revealing that multiple-knee spectra are common, constituting approximately half of all cortical recording sites (**Fig. 2c**). For these spectra with two knees, FOOOF algorithm may mischaracterize the higher-frequency knee as a series of oscillatory peaks, thereby generating spurious periodic components (right arrows, **Fig. 2d**, right). It can only separate oscillatory and aperiodic

components in a spectrum with a single knee (**Fig. 2d**, left).

To quantify this systematic bias, we compared knee estimates across all electrodes. For spectra identified as having one knee detected by the piecewise linear fitting, the two methods produced highly correlated knee frequencies (n = 3,107; r = 0.87, Pearson's r correlation; **Fig. 2e**). Critically, for two-knee spectra, FOOOF-derived knee values showed poor correlation with the lower-frequency knee identified by the piecewise method (n = 3,175; r = 0.19; **Fig. 2f**). These results demonstrated that single-knee fit overlooked higher-frequency knees by mislabeling it as oscillations and returned a biased estimate that failed to capture the dominant slow timescale. Thus, it was critical to apply the current method that did not assume the number of timescales on empirical data.

Functional gradients of multiple timescales in human sEEG

To determine whether cortical dynamics were organized along a singular or parallel temporal axis, we mapped intrinsic timescales across the human cortex using our validated pipeline. Analysis of a large sEEG dataset (n = 136 subjects) revealed that local dynamics are universally structured by two distinct temporal components. Whether an electrode exhibited one spectral knee or two, all estimated timescales segregated into a slow cluster (< ~1-10 Hz; **Fig. 3a-b**) and a fast cluster (~10-100 Hz; **Fig. 3c-d**). Formal model comparison confirmed that a two-component Gaussian mixture described this distribution better than a single- and triple- component model (ΔBIC > 18.2, see Methods), establishing a dual-timescale principle underlying cortical dynamics.

Crucially, these fast and slow components related to cortical hierarchy in fundamentally different ways. Projected onto two widely-studied cortical annotations, including the intrinsic functional gradients[33] and the unimodal-transmodal principle gradient[34] (**Fig. 3e-f**, left), slow timescales showed no systematic spatial variation (all p > 0.168, one-sided Pearson's correlation, FDR corrected; **Fig. 3e-f**, middle). In contrast, fast timescales exhibited a robust, monotonic gradient, decreasing from sensory to association regions (all p < 0.035, one-sided Pearson's correlation, FDR corrected; **Fig. 3e-f**, right). This dissociation remained significant after accounting for inter-electrode and inter-subject variance using linear mixed-effect models (fast component for both single- and double-knee spectrum: all β < -0.32, p < 0.0073).

Thus, the classical functional hierarchy was selectively embedded within the fast-temporal component. When we re-analyzed the same data using a standard single-knee fit (FOOOF), the relationship between timescales and cortical gradients disappeared (**Fig. S3**). The canonical hierarchy therefore emerged not from a unitary timescale gradient, but from a multi-scale architecture discernible only when fast and slow components are resolved.

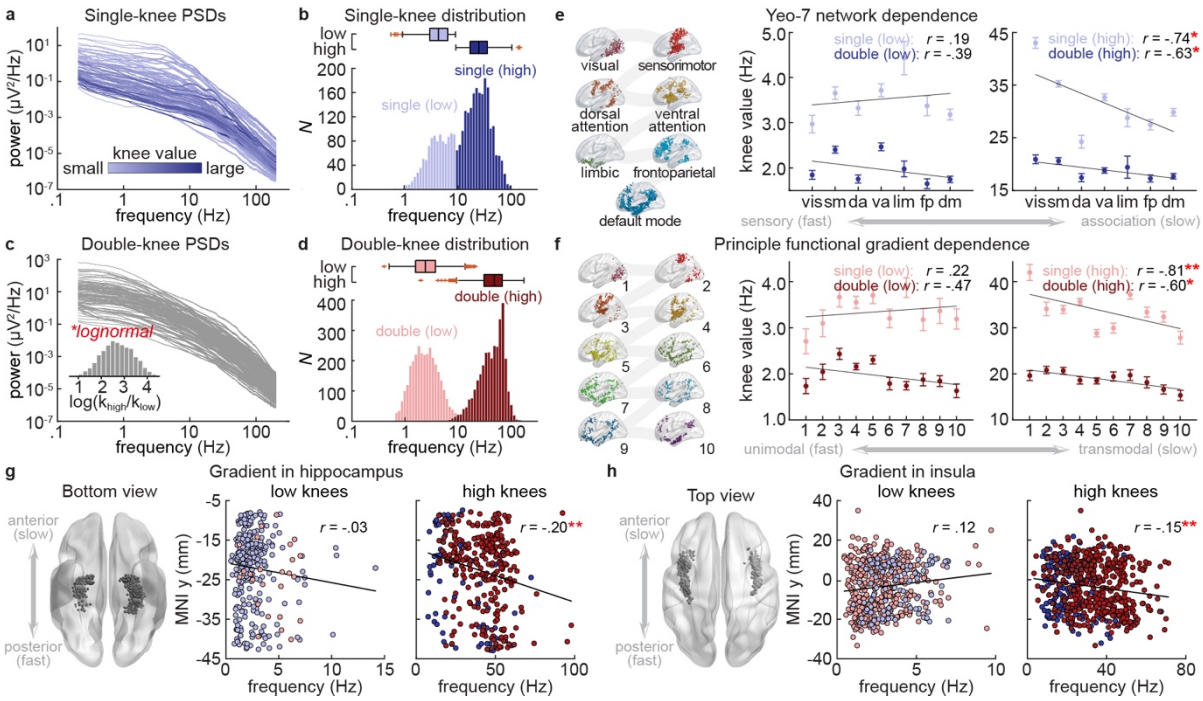

Figure 3. Dual-knee spectral organization in human sEEG

a, PSDs from single-knee contacts, color-coded by knee frequency.

b, Distribution of knee frequencies for single-knee spectra, revealing a pronounced bimodal structure separating low- and high-frequency components.

c, PSDs from double-knee contacts, showing spectra with two identifiable knees. The ratio between the two knees follows a lognormal distribution centered at ~2.5 (Lilliefors test, p = 0.001; inset)

d, Distributions of low- and high-frequency knees for double-knee spectra, forming the similar frequency range observed in single-knee spectra.

e-f, Spatial projection of low- and high-frequency knees onto the Yeo-7 intrinsic functional networks (**e**) and unimodal-to-transmodal principal gradient (**f**). Only high-frequency knees show functional gradient. Error bars denote s.e.m across electrode contacts.

g, High-frequency knees capture the canonical anterior-posterior timescale gradient in the hippocampus. Left, anatomical orientation showing anterior (slow) and posterior (fast) divisions. Middle, low-frequency knees show no systematic correlation with anatomical position. Right, high-frequency knees exhibit a significant negative correlation, with anterior contacts displaying slower timescales and posterior contacts faster ones.

h, High-frequency knees also reproduce the anterior-posterior gradient in the insula. Left, anatomical orientation showing anterior (slow) and posterior (fast) insular subdivisions. Middle, low-frequency knees show no significant gradient. Right, high-frequency knees conform to the expected slow-to-fast anterior-posterior organization. *p < 0.05, **p < 0.005.

High-frequency knees recovered in the insula and hippocampus

We next tested whether the principle of selective fast-timescale mapping generalizes to subcortical and allocortical structures with established anatomical gradients. We focused on the hippocampus[9,35] and the insula[36], where prior work has identified anterior-to-posterior gradients of timescales; Both regions were also commonly targeted in sEEG implantation

protocols. Consistent with our cortical findings, only the high-frequency knee captured these known gradients. In the hippocampus, high-frequency knee values decreased significantly from anterior to posterior (r = -0.21, p = 5×10^{-5}, one-sided Pearson's correlation; β = -0.134, p = 0.001, linear mixed-effects model; **Fig. 3g**), while low-frequency knees showed no systematic variation. An identical dissociation was observed in the insula, where the high-frequency knee similarly decreased along the anterior-posterior axis (r = -0.15, p = 2×10^{-4}, one-sided Pearson's correlation; β = -0.138, p = 1.2×10^{-4}, linear mixed-effects model; **Fig. 3h**). These results confirmed the selective mapping principle in classic gradients beyond the neocortex.

A conserved dual-knee architecture across conscious states

We further asked whether the segregation of cortical dynamics into distinct fast and slow timescales constituted a stable, intrinsic property of the cortex. To test its invariance across levels of consciousness, we tracked spectral knees within subjects across awake, resting, sleep, and anesthetic states. In every state, the bimodal separation remained intact (model comparison, ΔBIC > 5.4, see Methods; **Fig. 4a-c**). But both low- and high-frequency knees were highest in the awake state and decreased in less active states (all p < 0.012, bootstrap, FDR corrected; **Fig. 4d-f**), consistent with a reduced temporal integration window[10,37].

To assess stability at the level of individual sites, we tracked whether each site's spectrum was classified as single-knee or double-knee across states. More than half of sites retained the same class during transitions (**Fig. 4g-i**). Class changes occurred more frequently between awake and rest than between awake and sleep or anesthesia. Thus, these results suggested that the cortex-wide segregation into fast and slow timescales was stable across the continuum of consciousness, but local spectral profile was state-dependent.

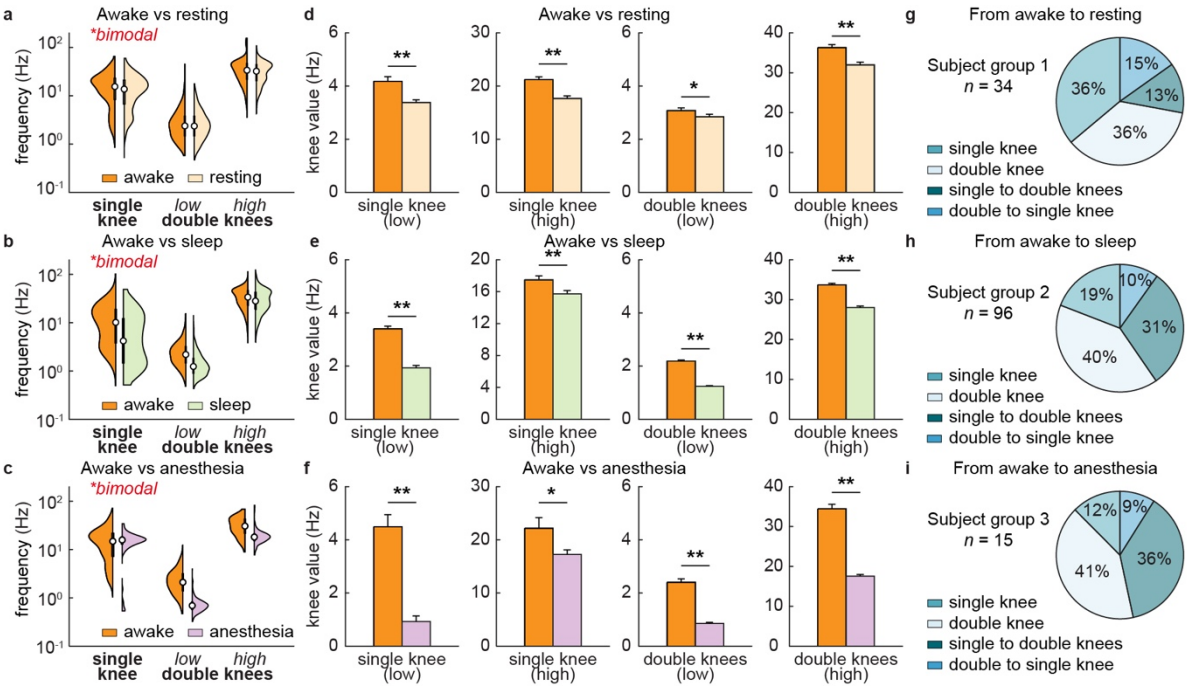

Figure 4. Conserved dual-knee spectral organization across consciousness states

a-c, Distributions of knee frequencies for single-knee spectra across states, showing a consistent bimodal organization into low- and high-frequency clusters. Knee frequencies of double-knee spectra map onto the same two clusters.
d-f, State-dependent changes in knee values. Both low- and high-frequency knees are highest in the awake state and decrease progressively in less active states. Error bars denote s.e.m across electrode contacts.
g-i, Transitions of spectral types (i.e., single-knee and double-knee) across awake to resting, sleep, and anesthesia states in three non-overlapping subject groups. More than half of contacts preserved their original spectral class, whereas the proportion of transitions differed by state. *$p < 0.05$, **$p < 0.005$.

Physiological origin for the low-frequency knee

Lastly, we sought to explain why the cortical functional gradient observed at higher frequencies was absent for the low-frequency knee component. Because the low-frequency knee clustered near the heart rate (mean ~1-2 Hz in the present dataset; ~1 Hz in prior work[21]) and heart rate variability can influence aperiodic spectral properties[38], these observations led us to test whether cardiac activity was related to the low-frequency knee and therefore uniformized its functional gradient. Using concurrent sEEG-ECG recordings (n = 40 subjects), we quantified ECG-sEEG coupling within knee defined frequency ranges (1-10 Hz for low knees and 10-100 Hz for high knees; **Fig. 5a**). Electrodes exhibiting a low-frequency knee showed significantly stronger ECG-sEEG correlations in the low-frequency band than electrodes without a low-frequency knee (p = 0.0003 for both comparisons, bootstrap, FDR corrected; **Fig. 5b**), whereas the presence of a high-frequency knee was not associated with ECG-sEEG coupling at higher frequencies. It therefore suggested that cardiac activity influenced the low-frequency knee through low-frequency coupling.

This ECG-sEEG coupling may arise either from ECG artefactual contamination or from genuine neurophysiological activity (i.e., heart-related evoked potentials, HEPs). We first applied a source separation (DDS) approach and showed no ECG-like artifacts in sEEG signals (**Fig. 5c**). Instead, heartbeat-locked analyses identified significant heartbeat-related activity in a subset of electrodes (red lines in **Fig. 5d**). A further alternative explanation was that these heartbeat-locked signals may reflect mechanical effects from nearby blood vessels rather than neural activity. To test this possibility, we reconstructed subject-specific vascular anatomy from angiography images and quantified the Euclidean distance between each sEEG contact and its nearest vessel surface. If vessel pulsation were the primary source of the observed HEPs, their magnitude should scale with proximity to vasculature. Contrary to this prediction, HEP amplitude showed no relationship with electrode-vessel distance (n = 474 electrodes; Pearson's $r = -0.027$, p = 0.55; linear mixed-effects model: β = -0.003, p = 0.10; **Fig. 5e**), arguing against a mechanical origin and supporting a neurophysiological interpretation.

We next exhibited the proportion of electrodes showing significant HEPs for each subject and cortical region (**Fig. 5f**). We reasoned that if the absence of a functional gradient at low frequencies were driven primarily by cardiac-related activity, excluding HEP-significant

electrodes might restore the gradient structure. However, even after removing these electrodes, low-frequency knee values remained uncorrelated with cortical functional hierarchies across both functional networks examined (all $p > 0.085$, one-sided Pearson's correlation; all $p > 0.157$, linear mixed-effects model; FDR corrected; **Fig. 5g**). These results suggested that the low-frequency knee is strongly influenced by physiological cardiac activity, reflecting a physiological timescale not canonical cortical functional gradient.

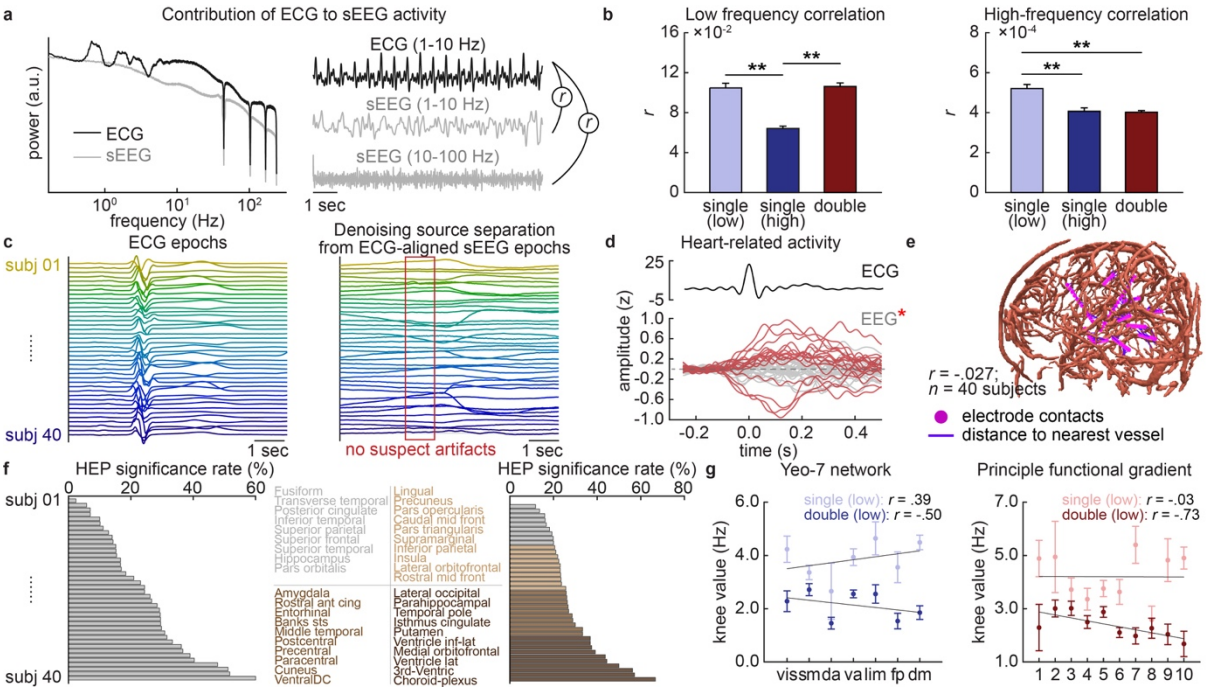

Figure 5. Cardiac-related neural activity selectively contributes to the low-frequency component.

a, Schematic of analysis. Left, representative power spectra of ECG (black) and sEEG (gray) illustrating that cardiac-related energy is concentrated at low frequencies. Right, example time-series traces showing ECG and band-limited sEEG signals used to quantify ECG-sEEG coupling within a low-frequency band (1-10 Hz, corresponding to low-frequency knees) and a higher-frequency band (10-100 Hz, corresponding to high-frequency knees).

b, ECG-sEEG correlation strength for the low-frequency band (left) and higher-frequency band (right), with contacts grouped by spectral class (single-knee and double-knee classes). Low-frequency ECG-sEEG coupling is selectively elevated in contacts exhibiting a low-frequency knee, whereas coupling in the higher-frequency band does not increase with the presence of a high-frequency knee. Bars and error bars denote group mean and s.e.m., respectively. $^{**}p < 0.005$.

c, Data-driven source separation (DDS) applied to sEEG epochs to assess potential ECG artefactual contamination. Left, R-peak-aligned ECG epochs across subjects. Right, corresponding DDS components derived from sEEG do not exhibit ECG-like waveforms (red box highlights the window where ECG features would be expected).

d, Heartbeat-related activity. Top, ECG waveform aligned to the R-peak. Bottom, Heartbeat-related activity from individual electrode contacts in an example subject, demonstrating significant neural responses time-locked to the cardiac cycle (red lines, $^{*}p < 0.05$).

e, Relationship between each contact's HEP magnitude and proximity to nearest vessel. Left, three-dimensional reconstruction of intracranial electrode contacts (plum-colored circles) overlaid on subject-specific vascular anatomy (red), with Euclidean distances computed to the nearest vessel surface. Right, scatter plot showing no significant correlation between HEP amplitude and electrode-vessel distance across contacts (Pearson's correlation and linear mixed-effects model), arguing against a mechanical or vascular vibration origin of the observed HEPs.

f, Distribution of significant HEPs across subjects and cortical regions. Left, proportion of electrode contacts exhibiting significant HEPs for each subject. Right, regional summary showing heterogeneous anatomical distribution of HEP-positive contacts across cortical areas.

g, Effect of excluding HEP-positive electrodes on functional gradients of low-frequency knee values. Low-frequency knee values remain uncorrelated with cortical functional hierarchy after removal of HEP-positive contacts in both functional networks examined, as assessed by Pearson's correlation and linear mixed-effects models (FDR corrected), indicating that cardiac-related activity alone does not account for the absence of a functional gradient at low frequencies.

Discussion

Our findings reveal that human cortical dynamics are organized around a stable, intrinsic duality of timescales, challenging the prevailing view of a unitary spectral hierarchy. We demonstrate a fundamental separation between a fast temporal component, which faithfully indexes the classic sensory-to-transmodal functional gradient, and a slow component, which appears to interface with systemic physiological rhythms. This multi-scale architecture requires a reassessment of how temporal subsystems support neural computation.

Many biological systems, including neural circuits, operate across multiple interacting time scales; when these scales are sufficiently separated, the dynamics can often be decomposed into coupled fast and slow subsystems[39]. The dual-timescale structure we observe is therefore broadly consistent with established biophysical frameworks[40-42]. The functional gradient captured by the high-frequency knee (~10-100 Hz, equivalent to ~1.6-16 ms) reveals a hierarchical organization of cortical processing speed. Notably, it is considerably faster than the timescales derived from single-neuron spike counts (tens to hundreds of milliseconds[8,18]), and from fMRI BOLD signals (seconds to minutes[2,9]). We suggest that these divergent gradients do not merely reflect different measurement modalities, but arise from distinct neurobiological substrates. Thus, the cortical hierarchy is best understood not as a single ladder, but as a system of parallel temporal channels serving distinct computational roles.

The slow component (~1-10 Hz) exhibits a distinct phenomenology, may acting as a bridge between neural dynamics and systemic physiology. Our data highlight a robust coupling between this low-frequency component and the electrocardiogram (**Fig. 5b**). Together with recent evidence linking cardiac activity to variations in aperiodic neural activity[38], this suggests that pulsatile hemodynamics may act as a physiological scaffold, transiently

modulating neuronal excitability and yielding a correlated decay in the macroscopic signal. Rather than viewing this coupling merely as artifactual contamination, we propose it represents a form of neuro-visceral integration[43], where systemic metabolic constraints or interoceptive feedback support global state regulation. This is consistent with the view that the brain's "slow" system is tasked with maintaining homeostasis and integrating organism-wide states, upon which the "fast" system executes precise computations[44].

This discovery was enabled by overcoming a core methodological constraint. While FOOOF remains one of the most accessible tools for aperiodic parameterization, its core limitation lies in a prior assumption of a single Lorentzian-derived knee (**Fig. 1**). Importantly, for non-invasive modalities such as EEG and MEG, single-knee assumption may be similarly misleading since a substantial proportion of second knees fall below 40 Hz. The current study proposes a practical pipeline for robust aperiodic feature extraction, including multiple knees and multi-slope spectral exponents, that mitigates these issues across electrophysiological modalities. Starting from pre-processed time-series data, we recommend applying IRASA to isolate oscillatory components. This method is largely parameter-free, and preserves the integrity of aperiodic component faithfully (**Fig. S1**). The cleaned signals are then transformed into power spectra using Welch's method. Note that sufficient window length is obligatory (**Fig. S2**), since short windows (e.g., 0.5-1 seconds[45-48]) are mathematically incapable of capturing slow timescales (no less than 1-2 Hz or even worse)[29-32]. Although the true knee frequency is unknown a priori, longer segments should be used to maximize the likelihood of resolving slowest timescales. Finally, the derived PSD can be fit using piecewise linear fit or dual-Lorentzian model[18] to explicitly resolve one or more timescales and their piecewise exponents.

Lastly, the emergence of dual-timescale architectures is reminiscent of what has been observed in oscillation and aperiodic exponent[19,24,25,27,47,49], and their relations to human cognitions[48,50,51], suggesting a need to characterize segregated spectral knee and exponents and their associated oscillations. These findings invite electrophysiological studies extended from the classic single-timescale estimate to investigating the aperiodic and periodic dynamics in temporal subsystems.

Methods

Simulating signals

Simulated PSD creation

To evaluate the performance of the piece-wise linear fitting procedure, we generated synthetic power spectra that contained predefined changes in spectral slope (i.e., multiple bend-knee points). These spectra were designed to avoid computational bias during and before PSD estimate while mimicking signals with heterogeneous timescales, such that each segment of the spectrum followed a distinct linear trend on a log-log scale. The ground-truth locations of the slope changes, as well as the slope values for each segment, were explicitly controlled and therefore known for every simulated spectrum. The simulated aperiodic PSD, $L(f)$, was defined as:

$$\log_{10} P(f) = \begin{cases} a_1 - \beta_1 \log_{10} f, & f_1 \le f < f_2 \\ a_2 - \beta_2 \log_{10} f, & f_2 \le f < f_3 \\ \vdots & \\ a_K - \beta_K \log_{10} f, & f_K \le f \le f_{K+1}, \end{cases}$$

where β_k denotes the ground-truth slope for segment $K \in \{1,2,3\}$, and a_k ensures continuity at the boundaries. Vertices frequencies and slope values were parameterized explicitly, enabling direct comparison between ground truth and algorithm estimates.

White noise was added independently at each frequency and scaled by a multiplicative factor m, producing the final simulated spectrum:

$$P_{\text{sim}}(f) = 10^{\log_{10} P(f)} + m\,\varepsilon(f),$$

where $\varepsilon(f)$ denotes Gaussian white noise. Noise levels spanned a predefined range to evaluate algorithm robustness under varying signal-to-noise conditions.

All spectra were simulated over 0.2 to 200 Hz with 0.2-Hz resolution. For each condition defined by number and value of knee points and noise level, A thousand spectra were generated. For each spectrum, we quantified (i) deviation between estimated and ground-truth knee values, (ii) the accuracy of recovering the correct number of knee points, and (iii) goodness of fit.

OU process with single timescale

To generate synthetic signals with a single intrinsic decay timescale, we simulated a one-dimensional Ornstein-Uhlenbeck process. The process satisfies the stochastic differential equation:

$$\tau dx(t) = -x(t)dt + \sigma d\xi(t)$$

where τ is the decay constant, σ describes the strength of noise, and $\xi(t)$ is the Brownian motion process. Numerical integration was performed using the Euler-Maruyama scheme:

$$x(t + \Delta t) = (1 - 1/\tau)x(t)dt + \sigma\eta(t)\sqrt{\Delta t}$$

with a step size of Δt = 0.001 s (i.e., 1 kHz sampling rate). Produced stationary OU signals exhibiting a single exponential decay in their autocorrelation structure.

OU process with double timescales

To construct synthetic signals containing two intrinsic timescales, we simulated a two-dimensional OU system and used the sum of its two components as the final observable signal. The system dynamics are given by:

$$d\vec{x} = \mathbf{A}\vec{x}dt + \mathbf{B}d\vec{\xi}(t)$$

with a diagonal system matrix and a noise strength matrix:

$$\mathbf{A} = \begin{bmatrix} -1/\tau_1 & 0 \\ 0 & -1/\tau_2 \end{bmatrix}$$

$$\mathbf{B} = \begin{bmatrix} \sigma_1 & 0 \\ 0 & \sigma_2 \end{bmatrix}$$

Thus, the two coordinates evolve as independent OU subprocesses with distinct decay constants

τ_1 and τ_2. The systems were integrated using the Euler-Maruyama update:

$$\vec{x}(t+\Delta t) = \vec{x}(t) + \mathbf{A}\vec{x}dt + \mathbf{B}\vec{\xi}(t)\sqrt{dt}$$

Each simulation began from $[0,0]^T$ and ran for 15 minutes at 1 kHz. The final signal was defined as the linear sum:

$$y(t) = \vec{c}\vec{x}(t)$$

Where $\vec{c}$ is the summation vector. This yields a process whose autocorrelation is the superposition of two exponential decays with timescales τ_1 and τ_2.

OU process with oscillation(s)

To generate signals exhibiting both stochastic decay and oscillatory structure, we extended the OU model by introducing a sinusoidal component to the OU signals described above. After simulating the OU system and forming the mixture signal $x_{\mathrm{OU}}(t)$, we added one or more oscillatory components of the form:

$$x_{\mathrm{osc}}(t) = A_{\mathrm{osc}} \sin(2\pi f_{\mathrm{osc}} t + \phi),$$

and final signal was constructed as:

$$x(t) = x_{\mathrm{OU}}(t) + x_{\mathrm{osc}}(t),$$

Taken together, all three kinds of OU synthetic time series combining single or double timescales, with or without oscillations, were used to evaluate the algorithm's ability to distinguish oscillatory component from aperiodic structure, and to test robustness under mixed periodic-stochastic conditions.

Empirical signals

Subject

This study analyzed fully de-identified intracranial EEG data originally collected for clinical monitoring in patients with medically intractable epilepsy at the Guangdong Sanjiu Brain Hospital (Guangzhou, China) and Shenzhen Second People's Hospital (Shenzhen, China). The present research involved secondary analysis of legacy clinical data and did not require any additional data collection or patient contact. All procedures were approved by the Research Ethics Committee of the two hospitals and the Institutional Review Board of New York University Shanghai.

A total of 175 patients (70 females; ages 18-52 years, mean age 29 years) were included. We analyzed three subsets of patients, each providing recordings from four physiological states to enable within-subject comparisons:: (i) awake dataset (136 subjects), consisting of patients with awake recordings; (ii) awake-asleep dataset (96 subjects), consisting of patients with both awake and sleep recordings; (iii) awake-resting-state dataset (34 subjects), consisting of patients with both awake and task-free resting-state recordings; and (iv) awake-anesthesia dataset (15 subjects), consisting of patients with both awake recordings and recordings acquired during anesthesia.

Physiological Recording States

Awake state: Awake recordings were collected when patients were fully conscious and responsive during routine clinical monitoring. Patients were not given behavioral instructions

and were free to engage in spontaneous everyday activities (e.g., quiet conversation, passive phone use). A 15-minute segment were extracted. In addition, for analyses relating the low-frequency knee to heart rate, we selected extended awake segments (30 mins to 4 hours) that contained concurrent ECG recordings.

Resting state: Resting-state recordings were obtained while patients were awake and instructed to relax without performing any task. Patients were asked to keep their eyes open or fixate on a visual point, remain still, and avoid speaking or moving. No sensory stimulation or cognitive tasks were presented. A 5-minute resting-state segments were used for analysis.

Asleep state: Sleep recordings were acquired during natural overnight clinical monitoring. For each patient, a 15-minute segment was randomly selected from natural sleep.

Anesthesia state: Anesthesia recordings were obtained during clinically indicated procedures in which anesthetic agents (e.g., propofol or sevoflurane, depending on clinical requirements) were administered by the clinical team. No task or stimulation was presented during anesthesia maintenance. A 15-minute segment was extracted for analysis.

sEEG data collection and preprocessing

Stereo-EEG was recorded with clinical depth electrodes (Sinovation, China) implanted in the brain parenchyma. Signals were amplified with a 256-channel Neuvo system and sampled at 2,000 Hz. Each lead comprised 8-16 cylindrical contacts (0.8 mm diameter; 2 mm length; 1.5 mm inter-contact spacing). Electrode trajectories were planned with the manufacturer's ROSA software by co-registering preoperative MRI and CT. Postoperative CT acquired with electrodes in place was then co-registered to the preoperative MRI to verify implantation accuracy relative to the planned paths. Electrode number and placement were determined solely on clinical grounds by the treating team to localize epileptogenic regions as part of presurgical evaluation.

All analyses were performed in custom MATLAB scripts[52,53]. Continuous sEEG was visually screened by a neurologist (J.C.) and analyst (Y.L. and H.M.) to identify epileptiform and artifactual activity. Data were resampled to 1,000 Hz; a narrow notch (48-52, 98-102, 148-152, and 198-202 Hz) removed line noise and its harmonics. Signals were then re-referenced with a local bipolar montage by differencing adjacent contacts on each shaft (the terminal contact was omitted). Channels labeled as white matter or as N/A by anatomical parcellation were excluded, and outlier channels were removed based on abnormally high mean amplitude.

Structural image and co-registration

For each patient, contact localization and anatomical labeling were performed in Brainstorm[54]. The T1 image was segmented with CAT12 and normalized to MNI152 space using SPM[55]. The postoperative CT was co-registered to the MRI with SPM12, and electrode contacts were manually identified on the co-registered image and their coordinates were

extracted in native MRI space. To obtain standardized anatomical locations, each contact's native-space coordinates were transformed into MNI152 space using the deformation fields estimated during MRI normalization. This procedure allowed an MNI coordinate for each contact for cortical-gradient analysis (see Cortical annotation).

ECG data processing

Concurrent ECG recordings were first notch filtered to remove line noise. R-peaks were detected using an automated peak-detection procedure and manually quality-checked to remove spurious detections and ectopic beats. To quantify ECG-sEEG coupling, sEEG and ECG were filtered into a low-frequency band (1-10 Hz) and a higher-frequency band (10-100 Hz), and Pearson correlations were computed between the band-limited ECG and each contact's band-limited sEEG over the continuous recordings. To assess whether ECG-sEEG coupling reflected direct ECG contamination versus heart-related neural activity, we additionally applied a data-driven source separation (DDS) procedure to isolate components maximally coupled to ECG and inspected heartbeat-centered averages for ECG-like morphology. Heart-related neural responses were evaluated by computing HEPs, obtained by averaging sEEG epochs time-locked to the ECG R-peak (baseline-corrected to the pre-R interval). Electrodes were labeled as HEP-significant using a two-sided bootstrap test across -200-0 ms baseline and 0-200 ms activity.

MR angiography

All vascular analyses began with raw magnetic resonance angiography (MRA) images. Vessel enhancement and segmentation were performed in 3D Slicer using a vesselness-based filter to improve contrast of tubular vascular structures against background tissue. Subject-specific vascular masks were then generated and were subsequently co-registered in SPM to each participant's T1-weighted anatomical image using a rigid-body transformation, ensuring spatial alignment across vascular, anatomical, and electrode coordinate spaces. Finally, three-dimensional surface models of the vasculature were reconstructed from the aligned masks via the marching cubes algorithm. Vertex coordinates of each model were converted into world coordinates using the appropriate affine transform, enabling consistent distance measurements between electrode locations and nearby vascular structures.

Timescale estimate pipeline

Fitting algorithm

Piecewise linear fitting: To identify multiple neural timescales in the aperiodic spectrum, we modeled PSD in log-log space, where 1/f-like spectra become approximately piecewise linear. The PSD estimate parameter and oscillation removal method were chosen to capture multiple spectral knees (**Table 1**). In this domain, each linear segment corresponds to a distinct power-law regime, and the transitions between segments, i.e., the spectral knees, defined characteristic timescales. Because the original frequency sampling is highly non-uniform in log space, with dense sampling at high frequencies and sparse sampling at low frequencies, direct fitting would overweight the high-frequency range. To ensure equal contribution across frequencies, the log-transformed PSD was linearly interpolated onto an

evenly spaced grid of 1,000 log-frequency points spanning the full fitting range (0.2-200 Hz). This procedure preserves the 1/f curvature while standardizing sampling density for segmentation.

For each contact, we fitted a piecewise linear model with K segments ($K = 1, \dots, 3$):

$$y(x) = \begin{cases} a_1 x + b_1, & x_1 \le x < c_1 \\ a_2 x + b_2, & c_1 \le x < c_2 \\ & \vdots \\ a_K x + b_K, & c_{K-1} \le x \le x_K, \end{cases}$$

where a_k were local slopes and c_j were internal breakpoints. The negative slopes ($\beta_k = -a_k$) represented local aperiodic exponents, while breakpoints defined knee frequencies $f_{\text{knee}} = 10^{c_j}$.

To avoid enforcing a predetermined number of knees, we selected the optimal number of segments K by minimizing a penalized objective that traded off goodness-of-fit and model complexity. The regularization weight λ was chosen through systematic qualitative assessment that best preserved true curvature without over-segmentation. This fixed λ was then applied uniformly across all contacts. For each candidate $K = 1, \dots, 3$, the penalized loss was estimated using Bayesian optimization, and the model was refit using the optimal K^*. Internal breakpoints were extracted as knee frequencies, and corresponding slopes. This procedure allowed, for every electrode, the number of knees, their frequencies in Hz, and the associated spectral exponents, forming the basis for all subsequent timescale analyses.

Autocorrelation fitting: Autocorrelation-based timescale estimates were obtained by fitting exponential decay models to the broadband ACF of each sEEG electrode contact. Continuous data were segmented into overlapping windows (50% overlap), with window lengths chosen to capture slow dynamics (**Table 1**). Within each window, the ACF was computed using FFT-based estimation up to the maximum lag, and windowed ACFs were averaged to yield a stable mean ACF. The fitting range was restricted to the portion of the ACF above 0 of its maximum to avoid contamination from long-lag noise. For empirical data, we fitted a shifted exponential of the form

$$R(t) \approx A\left(e^{-t/\tau} + B\right),$$

where τ is the autocorrelation timescale and B captures residual slow drifts. Parameters were estimated via differential evolution using broad bounds, and non-convergent fits were excluded. For simulated signals containing two ground-truth timescales, we additionally fitted a bi-exponential model,

$$R(t) \approx A_1 e^{-t/\tau_1} + (1 - A_1) e^{-t/\tau_2} + B,$$

with $A_1 \in (0,1)$ enforcing a convex mixture of two components. This dual-exponential model was used solely to validate the behavior of ACF estimators under multiscale dynamics and was not applied to human data.

FOOOF fitting: For comparison with single-knee models, we fit each power spectrum using the FOOOF algorithm[20], which parameterizes the aperiodic component using a Lorentzian 1/f function and Gaussian peaks. FOOOF was applied across simulations and empirical data

analysis using the following parameters: knee mode, a maximum of three oscillatory peaks (max_n_peaks = 3), peak width limits of 1-12 Hz (peak_width_limits=[1, 12]), a minimum peak height of 0.2 (min_peak_height = 0.2), and a peak-detection threshold of 2 (peak_threshold = 2). All spectra were fit over the 0.2-200 Hz frequency range.

Oscillatory activity removal

Oscillatory components were removed using the Irregular-Resampling Auto-Spectral Analysis procedure[28], which separated the broadband aperiodic spectrum from narrowband rhythmic peaks through non-integer resampling. For each sEEG electrode contact, continuous data were divided into 70-s windows (**Table 1**), and the signal was resampled using a set of multiplicative factors h and 1/h (e.g., $h = 1.1, 1.2, ...$), stretching and compressing oscillatory components while leaving the fractal 1/f background unchanged. Averaging the spectra across all resampling factors canceled out the oscillatory components, yielding a fractal (aperiodic) spectrum; subtracting this from the original power spectrum produces an estimate of the oscillatory residual. IRASA was applied over 0.01-400 Hz (due to algorithmic requirement) using the same sampling rate and windowing parameters as the PSD computation, and the fractal spectrum was taken forward for knee fitting.

FOOOF-based oscillation removal was also used only for comparison, using the above-mentioned parameters. The aperiodic component estimated by FOOOF was subtracted from the original PSD to obtain a second oscillation-removed spectrum used solely for cross-method validation.

Table 1. Summary of datasets and analysis configurations

Data	Window length	Oscillation removal method	Fitting methods	Relevant figures
PSD simulations	-	-	Piecewise-linear	**Fig. 2a-b**
Awake data (*n* = 136)	70s, 50% overlap	FOOOF	FOOOF	**Fig. 2d-f**
	70s, 50% overlap	FOOOF	Piecewise-linear	**Fig. 2c, e-f**
Awake data (*n* = 136)	70s, 50% overlap	IRASA	Piecewise-linear	**Fig. 3**
Awake and resting-state data (*n* = 34)				**Fig. 4ad**
Awake and asleep data (*n* = 96)				**Fig. 4be**
Awake and anesthesia data (*n* = 15)				**Fig. 4cf**

OU simulation with oscillations	5s, 50% overlap	FOOOF	Piecewise-linear	**Fig. S1**
	5s, 50% overlap	IRASA	Piecewise-linear	**Fig. S1**
OU simulation with multiple timescale(s)	1-100s, 50% overlap	-	Piecewise-linear	**Fig. S2a, c**
	1-100s, 50% overlap	-	Autocorrelation	**Fig. S2b, d**
Awake data (*n* = 136)		FOOOF	FOOOF	**Fig. S3**

Cortical annotation

To place local timescale estimates within established macroscale organization, we examined their distribution across two widely used cortical atlases: the seven intrinsic functional networks[33], and the principal unimodal-transmodal functional gradient[9]. For each atlas, electrodes belonging to the same gradient bin were grouped, and low- and high-frequency knees were averaged separately within each group. These complementary annotations capture distinct aspects of cortical hierarchy and provide a principled framework for assessing large-scale organization in spectral timescales.

Statistical analysis

All statistical comparisons were conducted within subjects, and false discovery rate (FDR) correction was applied to control for multiple comparisons.

Bootstrap test

Bias-corrected and accelerated bootstrapping[56] was used to compare difference between conditions (**Fig. 4d-f** and **Fig. 5b**). In the bootstrap procedure, participants were resampled 10,000 times with replacement. For each comparison, we calculated the proportion A of bootstrap samples in which the mean knee value in one condition was greater (or smaller) than in the other condition. All tests were two-sided, with formular to obtain p-value: $p = (2 \cdot \min(A, 1 - A) \cdot 10{,}000 + 1)/10{,}001$.

Bimodal distribution test

To assess whether the data exhibited a unimodal or bimodal distribution, we adopted a model-based approach using Gaussian mixture models. The data were first log-transformed, after which Gaussian mixture models with one to four components were fitted using the expectation-maximization algorithm. To ensure robust parameter estimation, each model was fitted with multiple random initializations, and covariance regularization was applied to avoid numerical instability. Model selection was performed using the Bayesian Information Criterion, which balances goodness of fit against model complexity. If the model with two components yielded the lowest BIC, indicating that a bimodal distribution provided the most parsimonious explanation of the data.

Correlation analysis

Pearson's correlation was used to quantify associations between spectral knee frequency and the cortical functional gradient (**Fig. 3e-f**), between knees estimated using FOOOF and piecewise-linear fitting (**Fig. 1e-f**), and between sEEG and ECG time series (**Fig. 5**).

Linear mixed effect model

To complement correlation analyses and account for repeated measurements across channels and subjects, we further performed linear mixed-effects (LME) modeling. Functional gradient was entered as a fixed effect, while subject- and channel-level variability were modeled as random intercepts, with channels nested within subjects. For the relation between knee and gradient, we used equation: $\mathrm{knee} \sim \mathrm{gradient} + (1 \mid \mathrm{subject{:}\,channel})$; for the relation between HEP amplitude and Euclidean distance to vessel, we used equation: $\mathrm{HEP} \sim \mathrm{distance} + (1 \mid \mathrm{subject{:}\,channel})$. Models were fitted using MATLAB's fitlme function.

Data availability

The de-identified sEEG datasets supporting the findings of this study are available at http://github.com/. Raw data containing identifiable information can be made available from the corresponding author upon request and subject to institutional data-sharing agreements.

Code availability

The code supporting the findings of this study are available at our GitHub repository: https://github.com/. The algorithm code is openly available for both MATLAB and python version: https://slang.science/, and includes a documentation site: https://slang.science/.

Acknowledgement

We sincerely thank Youcun Zheng, Yiduo Lu, Ruoyu Wu and Peiyu He for assisting in data preparation. This study is supported by the National Natural Science Foundation of China 32271101 (X.T.), the National Science and Technology Innovation STI2030-Major Project No. 2022ZD0204600 and the Natural Science Foundation of China through Grant No. 31771147 (Z.L. and L.T.), and Program of AI-Driven Initiative to Promote Research Paradigm Reform and Empower Disciplinary Advancement by Shanghai Municipal Education Commission (SMEC), Program of Introducing Talents of Discipline to Universities, Base B16018, and NYU Shanghai Boost Fund to X.T.

Author contributions

All authors initiated and designed the study. Y.L. and H.M. conceived of and coded the algorithm. Y.L., H.M., Z.L., and Q.L. contributed code and tested the algorithm against real and simulated data. J.C. and Y.C. collected data. Y.L. and H.M. analyzed data. L.T, Z.X. and X.Z. provided overall supervision and guidance throughout the project. All authors contributed to the manuscript.

Declaration of interests

The authors declare no competing financial interests.

References

1 Honey, C. J. *et al.* Slow cortical dynamics and the accumulation of information over long timescales. *Neuron* **76**, 423–434 (2012).
2 Hasson, U., Yang, E., Vallines, I., Heeger, D. J. & Rubin, N. A hierarchy of temporal receptive windows in human cortex. *Journal of neuroscience* **28**, 2539–2550 (2008).
3 Giraud, A.-L. & Poeppel, D. Cortical oscillations and speech processing: emerging computational principles and operations. *Nature neuroscience* **15**, 511–517 (2012).
4 Miller, J. A. & Constantinidis, C. Timescales of learning in prefrontal cortex. *Nature Reviews Neuroscience* **25**, 597–610 (2024).
5 Pritchard, W. S. The brain in fractal time: 1/f-like power spectrum scaling of the human electroencephalogram. *Int J Neurosci* **66**, 119–129 (1992). https://doi.org/10.3109/00207459208999796
6 Hausdorff, J. M. & Peng, C. Multiscaled randomness: A possible source of 1/f noise in biology. *Phys Rev E Stat Phys Plasmas Fluids Relat Interdiscip Topics* **54**, 2154–2157 (1996). https://doi.org/10.1103/physreve.54.2154
7 He, B. J. Scale-free brain activity: past, present, and future. *Trends Cogn Sci* **18**, 480–487 (2014). https://doi.org/10.1016/j.tics.2014.04.003
8 Murray, J. D. *et al.* A hierarchy of intrinsic timescales across primate cortex. *Nat Neurosci* **17**, 1661–1663 (2014). https://doi.org/10.1038/nn.3862
9 Raut, R. V., Snyder, A. Z. & Raichle, M. E. Hierarchical dynamics as a macroscopic organizing principle of the human brain. *Proc Natl Acad Sci U S A* **117**, 20890–20897 (2020). https://doi.org/10.1073/pnas.2003383117
10 Wolff, A. *et al.* Intrinsic neural timescales: temporal integration and segregation. *Trends Cogn Sci* **26**, 159–173 (2022). https://doi.org/10.1016/j.tics.2021.11.007
11 Soltani, A., Murray, J. D., Seo, H. & Lee, D. Timescales of Cognition in the Brain. *Curr Opin Behav Sci* **41**, 30–37 (2021). https://doi.org/10.1016/j.cobeha.2021.03.003
12 Wu, K. & Gollo, L. L. Mapping and modeling age-related changes in intrinsic neural timescales. *Commun Biol* **8**, 167 (2025). https://doi.org/10.1038/s42003-025-07517-x
13 Golesorkhi, M., Gomez-Pilar, J., Tumati, S., Fraser, M. & Northoff, G. Temporal hierarchy of intrinsic neural timescales converges with spatial core-periphery organization. *Commun Biol* **4**, 277 (2021). https://doi.org/10.1038/s42003-021-01785-z
14 Cavanagh, S. E., Wallis, J. D., Kennerley, S. W. & Hunt, L. T. Autocorrelation structure at rest predicts value correlates of single neurons during reward-guided choice. *Elife* **5**, e18937 (2016). https://doi.org/10.7554/eLife.18937
15 Siegle, J. H. *et al.* Survey of spiking in the mouse visual system reveals functional hierarchy. *Nature* **592**, 86–92 (2021). https://doi.org/10.1038/s41586-020-03171-x
16 Wilting, J. & Priesemann, V. Inferring collective dynamical states from widely unobserved systems. *Nat Commun* **9**, 2325 (2018). https://doi.org/10.1038/s41467-018-04725-4
17 Li, G., Li, S. & Wang, X.-J. A hierarchy of time constants and reliable signal propagation in the marmoset cerebral cortex. *Nature Communications* (2025). https://doi.org/10.1038/s41467-025-66699-4
18 Gao, R., van den Brink, R. L., Pfeffer, T. & Voytek, B. Neuronal timescales are functionally dynamic and shaped by cortical microarchitecture. *Elife* **9**, e61277 (2020). https://doi.org/10.7554/eLife.61277
19 Wilson, L. E., da Silva Castanheira, J. & Baillet, S. Time-resolved parameterization of aperiodic

and periodic brain activity. *Elife* **11**, e77348 (2022). https://doi.org/10.7554/eLife.77348

20 Donoghue, T. *et al.* Parameterizing neural power spectra into periodic and aperiodic components. *Nat Neurosci* **23**, 1655–1665 (2020). https://doi.org/10.1038/s41593-020-00744-x

21 He, B. J., Zempel, J. M., Snyder, A. Z. & Raichle, M. E. The temporal structures and functional significance of scale-free brain activity. *Neuron* **66**, 353–369 (2010). https://doi.org/10.1016/j.neuron.2010.04.020

22 Miller, K. J., Sorensen, L. B., Ojemann, J. G. & den Nijs, M. Power-law scaling in the brain surface electric potential. *PLoS Comput Biol* **5**, e1000609 (2009). https://doi.org/10.1371/journal.pcbi.1000609

23 Freeman, W. J. & Zhai, J. Simulated power spectral density (PSD) of background electrocorticogram (ECoG). *Cogn Neurodyn* **3**, 97–103 (2009). https://doi.org/10.1007/s11571-008-9064-y

24 Lendner, J. D., Lin, J. J., Larsson, P. G. & Helfrich, R. F. Multiple Intrinsic Timescales Govern Distinct Brain States in Human Sleep. *J Neurosci* **44**, e0171242024 (2024). https://doi.org/10.1523/JNEUROSCI.0171-24.2024

25 Gerster, M. *et al.* Separating Neural Oscillations from Aperiodic 1/f Activity: Challenges and Recommendations. *Neuroinformatics* **20**, 991–1012 (2022). https://doi.org/10.1007/s12021-022-09581-8

26 Donoghue, T. *et al.* Evaluating and Comparing Measures of Aperiodic Neural Activity. *bioRxiv* (2024). https://doi.org/10.1101/2024.09.15.613114

27 Donoghue, T., Schaworonkow, N. & Voytek, B. Methodological considerations for studying neural oscillations. *Eur J Neurosci* **55**, 3502–3527 (2022). https://doi.org/10.1111/ejn.15361

28 Wen, H. & Liu, Z. Separating Fractal and Oscillatory Components in the Power Spectrum of Neurophysiological Signal. *Brain Topogr* **29**, 13–26 (2016). https://doi.org/10.1007/s10548-015-0448-0

29 Zeraati, R., Engel, T. A. & Levina, A. A flexible Bayesian framework for unbiased estimation of timescales. *Nat Comput Sci* **2**, 193–204 (2022). https://doi.org/10.1038/s43588-022-00214-3

30 Afyouni, S., Smith, S. M. & Nichols, T. E. Effective degrees of freedom of the Pearson's correlation coefficient under autocorrelation. *NeuroImage* **199**, 609–625 (2019). https://doi.org/10.1016/j.neuroimage.2019.05.011

31 Bartlett, M. S. On the Theoretical Specification and Sampling Properties of Autocorrelated Time-Series. *J Roy Stat Soc B* **8**, 27–41 (1946).

32 Marom, S. Neural timescales or lack thereof. *Prog Neurobiol* **90**, 16–28 (2010). https://doi.org/10.1016/j.pneurobio.2009.10.003

33 Schaefer, A. *et al.* Local-Global Parcellation of the Human Cerebral Cortex from Intrinsic Functional Connectivity MRI. *Cereb Cortex* **28**, 3095–3114 (2018). https://doi.org/10.1093/cercor/bhx179

34 Margulies, D. S. *et al.* Situating the default-mode network along a principal gradient of macroscale cortical organization. *Proc Natl Acad Sci U S A* **113**, 12574–12579 (2016). https://doi.org/10.1073/pnas.1608282113

35 Rait, L. I., Wanjia, G., Ye, Z., DuBrow, S. & Kuhl, B. A. Hippocampal Drift Rate Reflects the Temporal Organization of Memories. *The Journal of Neuroscience* **45**, e0909252025 (2025). https://doi.org/10.1523/jneurosci.0909-25.2025

36 Livneh, Y. & Andermann, M. L. Cellular activity in insular cortex across seconds to hours:

Sensations and predictions of bodily states. *Neuron* **109**, 3576–3593 (2021).
37 Senkowski, D. & Engel, A. K. Multi-timescale neural dynamics for multisensory integration. *Nat Rev Neurosci* **25**, 625–642 (2024). https://doi.org/10.1038/s41583-024-00845-7
38 Schmidt, F. *et al.* Age-related changes in 'cortical' 1/f dynamics are linked to cardiac activity. *Elife* **13**, RP100605 (2025). https://doi.org/ARTN RP100605
10.7554/eLife.100605
39 Bertram, R. & Rubin, J. E. Multi-timescale systems and fast-slow analysis. *Mathematical biosciences* **287**, 105–121 (2017).
40 Marom, S. & Marder, E. A biophysical perspective on the resilience of neuronal excitability across timescales. *Nature Reviews Neuroscience* **24**, 640–652 (2023).
41 Gjorgjieva, J., Drion, G. & Marder, E. Computational implications of biophysical diversity and multiple timescales in neurons and synapses for circuit performance. *Current opinion in neurobiology* **37**, 44–52 (2016).
42 Coombes, S. Large-scale neural dynamics: simple and complex. *NeuroImage* **52**, 731–739 (2010).
43 Shmueli, K. *et al.* Low-frequency fluctuations in the cardiac rate as a source of variance in the resting-state fMRI BOLD signal. *Neuroimage* **38**, 306–320 (2007). https://doi.org/10.1016/j.neuroimage.2007.07.037
44 Buzsaki, G. Large-scale recording of neuronal ensembles. *Nat Neurosci* **7**, 446–451 (2004). https://doi.org/10.1038/nn1233
45 Cusinato, R. *et al.* Intrinsic Neural Timescales in the Temporal Lobe Support an Auditory Processing Hierarchy. *J Neurosci* **43**, 3696–3707 (2023). https://doi.org/10.1523/JNEUROSCI.1941-22.2023
46 Cusinato, R., Seiler, A., Schindler, K. & Tzovara, A. Sleep Modulates Neural Timescales and Spatiotemporal Integration in the Human Cortex. *J Neurosci* **45** (2025). https://doi.org/10.1523/JNEUROSCI.1845-24.2025
47 Bush, A., Zou, J. F., Lipski, W. J., Kokkinos, V. & Richardson, R. M. Aperiodic components of local field potentials reflect inherent differences between cortical and subcortical activity. *Cereb Cortex* **34** (2024). https://doi.org/10.1093/cercor/bhae186
48 Raposo, I. *et al.* Human attention-guided visual perception is governed by rhythmic oscillations and aperiodic timescales. *PLoS Biol* **23**, e3003232 (2025). https://doi.org/10.1371/journal.pbio.3003232
49 Brake, N. *et al.* A neurophysiological basis for aperiodic EEG and the background spectral trend. *Nat Commun* **15**, 1514 (2024). https://doi.org/10.1038/s41467-024-45922-8
50 Brookshire, G. Putative rhythms in attentional switching can be explained by aperiodic temporal structure. *Nat Hum Behav* **6**, 1280–1291 (2022). https://doi.org/10.1038/s41562-022-01364-0
51 Preston, M., Jr., Schaworonkow, N. & Voytek, B. Time-Resolved Aperiodic and Oscillatory Dynamics during Human Visual Memory Encoding. *J Neurosci* **45** (2025). https://doi.org/10.1523/JNEUROSCI.2404-24.2025
52 Lu, Y., Jin, P., Ding, N. & Tian, X. Delta-band neural tracking primarily reflects rule-based chunking instead of semantic relatedness between words. *Cereb Cortex* **33**, 4448–4458 (2023). https://doi.org/10.1093/cercor/bhac354
53 Lu, Y., Jin, P., Pan, X. & Ding, N. Delta-band neural activity primarily tracks sentences instead of semantic properties of words. *Neuroimage* **251**, 118979 (2022).

https://doi.org/10.1016/j.neuroimage.2022.118979

54 Tadel, F., Baillet, S., Mosher, J. C., Pantazis, D. & Leahy, R. M. Brainstorm: a user-friendly application for MEG/EEG analysis. *Comput Intell Neurosci* **2011**, 879716 (2011). https://doi.org/10.1155/2011/879716

55 Tzourio-Mazoyer, N. *et al.* Automated anatomical labeling of activations in SPM using a macroscopic anatomical parcellation of the MNI MRI single-subject brain. *Neuroimage* **15**, 273–289 (2002). https://doi.org/10.1006/nimg.2001.0978

56 Efron, B. & Tibshirani, R. J. *An Introduction to the Bootstrap*. (CRC press, 1994).